Advanced Electronic Materials

ADVANCED ELECTRONIC MATERIALS Open Access

www.advelectronicmat.de

RESEARCH ARTICLE OPEN ACCESS

Role of Rare-Earth Lanthanum Doping on Electrical Performance and Stability of Atomic Layer Deposition Processed Indium Oxide Thin-Film Transistors

Jinxiu Zhao | Zhiyu Lin | Ziheng Wang | Liankai Zheng | Kai Jiang | Haoran Zhao | Mengwei Si

The National Key Laboratory of Advanced Micro and Nano Manufacture Technology and School of Electronic Information and Electrical Engineering, Shanghai Jiao Tong University, Shanghai, China

Correspondence: Mengwei Si (mengwei.si@sjtu.edu.cn)

Received: 16 December 2025 | **Revised:** 4 February 2026 | **Accepted:** 2 March 2026

Keywords: atomic layer deposition | bias stress stability | rare-earth doping | thin-film transistors

ABSTRACT

In this work, lanthanum-doped indium oxide (InLaO) thin-film transistors (TFTs) are fabricated by atomic layer deposition (ALD) with different La concentrations. Effects of La concentration on crystallinity, surface chemical information, surface morphology, along with the electrical properties of ALD-grown InLaO TFTs, are systematically investigated. With increasing La content from 0 to 20.2 at. %, the field-effect mobility (μ_{FE}) continuously decreases from 106.3 to 2.3 $cm^2(V{\cdot}s)^{-1}$. In contrast, the negative bias stability (NBS) is remarkably enhanced, and the threshold voltage (V_{TH}) shifts from −0.157 to −0.005 V under −2 V bias stress for 1000 s. This trend is attributed to the stronger La—O bonding energy compared to In—O. The stable La—O bonds effectively suppress the generation of oxygen vacancies (V_O) and associated defect states, which explains the superior stability. Concurrently, these bonds also restrain the formation of conduction pathways, leading to the observed mobility degradation. This work demonstrates that La doping is an effective strategy to precisely tune the stability-mobility balance in oxide TFTs.

1 | Introduction

Since the discovery of amorphous indium gallium zinc oxide (a-IGZO), a-IGZO TFTs act as an important switching control device of backplane technology for modern high-resolution active-matrix displays, owing to relatively high mobility, excellent uniformity, and optical transparency [1–8]. However, next-generation display technology like flexible displays and micro-LED needs superior TFT performance [9, 10]. A critical issue for metal oxide TFTs is bias stress instability, which damages pixel fidelity and long-term device reliability [11, 12]. The instability is mainly attributed to intrinsic defects at the channel and channel/gate insulator (GI) interface, which can trap or release carriers under different stress conditions. The defects include oxygen vacancies (V_O), weakly bonded O, undercoordinated O, and Hydrogen-related defects, in which V_O is the most prevalent and influential defect [13–15].

Among various amorphous oxide semiconductors (AOS), indium oxide (In_2O_3) has an attractive prospect due to its high intrinsic electron mobility coming from the large spatial overlap of In 5s orbitals [7, 16]. However, its practical application is severely affected by the high density of V_O. These vacancies act as shallow donors, leading to excessive carrier concentration, poor turn-off characteristics, and obvious bias stress instability [17, 18]. Therefore, effective defect engineering to suppress V_O while maintaining reasonable mobility is necessary for advancing In_2O_3-based electronics.

TABLE 1 | Spectroscopic ellipsometry-based thickness and XPS-based La atomic ratio (La/(La+In)) of the InLaO film according to the ALD super-cycle and cycle number of In_2O_3 and La_2O_3.

Sample	Super-cycle (In+La)	Number of super-cycle	Thickness [nm]	La [at. %]
In_2O_3	—	85	4.0	0
$In_{1.8}La_{0.2}O_3$	25+1	7	8.4	10.8
$In_{1.7}La_{0.3}O_3$	15+1	11	8.4	15.6
$In_{1.6}La_{0.4}O_3$	10+1	15	8.2	20.2

Doping with stronger-bonding cations has proven to be a viable strategy for defect modulation in oxides [19–22]. In this case, La, a rare-earth element, presents a compelling choice. The La^{3+} has a significantly larger ionic radius (~1.032 Å) compared to In^{3+} (~0.80 Å), and the La–O bond energy (~802 kJ mol^{-1}) is substantially greater than that of In–O (~346 kJ mol^{-1}). These intrinsic properties indicate that La incorporation could frustrate the crystallization of In_2O_3, promote amorphous phase formation for better uniformity, and most importantly, suppress the formation of V_O and decrease the concentration of trap states through the formation of more stable metal-oxygen bonds, thereby enhancing bias stability. La doping in solution-processed or sputtered InLaO TFTs has been explored, while a systematic investigation with atomic layer deposition (ALD) has rarely been reported [23–31]. Because of its exceptional conformality, thickness control, and low-temperature processing, ALD has been widely used in integrated circuits. While ALD faces challenges in growth rate, cost, and relatively complex precursors compared to sputtering and solution processes, the layer-by-layer growth enabled by ALD provides an ideal way to achieve precise and uniform cationic doping and high quality films growth.

This work presents a comprehensive study on La doping of ALD-grown In_2O_3 thin films for high-stability TFT applications for the first time. ALD-cycle engineering was used to achieve precise and wide-range La doping concentrations from 0 to 20 at. %. grazing incidence X-ray diffraction (GIXRD), X-ray photoelectron spectroscopy (XPS), and atomic force microscopy (AFM) were employed to characterize the La-induced structural, chemical, and morphological changes related to the performance of InLaO TFTs. We demonstrated that La doping effectively passivates V_O, induces a crystalline-to-amorphous transition, and modulates the electrical properties. The fabricated InLaO TFTs exhibit excellent channel/GI interface with near-ideal subthreshold swing (SS). More significantly, we achieved high bias stress stability under high electric fields, exceeding previously reported La-doped In_2O_3 devices. This work establishes ALD as a powerful tool for rare-earth doping in metal oxide and provides a pathway to designing reliable, high-performance devices through defect engineering.

2 | Results and Discussion

2.1 | Characterization of InLaO Thin Films

The spectroscopic ellipsometry-based thickness and XPS-based cation composition of the InLaO film are shown in Table 1. Despite varying total cycle numbers, the thickness of all three InLaO films was similar (~8 nm). This result is attributed to the designed super-cycle, wherein the final thickness is a sum of the growth from single In_2O_3 and La_2O_3 sub-cycles. The measured growth rates of In_2O_3 and La_2O_3 were 0.44 and 1.1 Å/cycle in InLaO, respectively, aligning with findings in the literature [32, 33]. In_2O_3 growth rate of 0.47 Å/cycle was measured in the In_2O_3 process, similar to the growth rate in InLaO. Correspondingly, the La atomic concentration, defined as the atomic radio of La to (In + La), decreases gradually from 20.2 to 10.8 at. % with the proportion of In_2O_3 sub-cycles in the ALD sequence increased. This trend confirms that the cation composition (In/La ratio) can be effectively tuned by adjusting the sub-cycle ratio of the metal oxides.

AFM topological images of the InLaO thin film with different concentrations are shown in Figure 1a–e. The Root Mean Square roughness (RMS) values of the $In_{1.6}La_{0.4}O_3$, $In_{1.7}La_{0.3}O_3$, $In_{1.8}La_{0.2}O_3$, and In_2O_3 films are estimated to be 0.45, 0.40, 0.33, and 0.29 nm, respectively. Although the incorporation of La leads to a mild increase in surface roughness compared to the undoped film, the surfaces of InLaO films are smooth. Such low surface roughness is essential for high-performance devices, as it effectively reduces carrier scattering at the interface [34]. The crystallinity of InLaO films annealing in O_2 at 400°C for 10 min was examined using grazing incidence X-ray diffraction measurement, as shown in Figure 3f. The In_2O_3 film showed a polycrystalline phase exhibiting dominant diffraction peaks at 2θ values of 30.58°, corresponding to the (222) diffraction peaks. In contrast, all La-doped films showed an amorphous phase, suggesting that La could frustrate In_2O_3 crystallization. The transition from a polycrystalline to an amorphous phase with La doping can be mechanistically understood through a combination of crystallographic constraints and thermodynamic. According to the Hume-Rothery rules, when the radius difference between dopant and host ions is greater than ~15% severely limits substitutional compound formation [35]. In this case, the ionic radius of La^{3+} (~1.03 Å) is approximately 29% larger than that of In^{3+} (~0.80 Å), far exceeding the threshold. This severe mismatch makes the incorporation of La^{3+} into the In_2O_3 lattice highly energetically unfavorable, preventing the development of a periodic crystalline structure. Besides, the significantly higher bond strength of La—O compared to In—O creates substantial energy barriers for atomic rearrangement during thermal annealing. These stable La—O bonds effectively pin local atomic configurations, hindering the long-range diffusion and ordering necessary for crystallization. Consequently, the strong La—O bonding and the large ionic size frustrate the crystallization and stabilize the amorphous phase of the InLaO films.

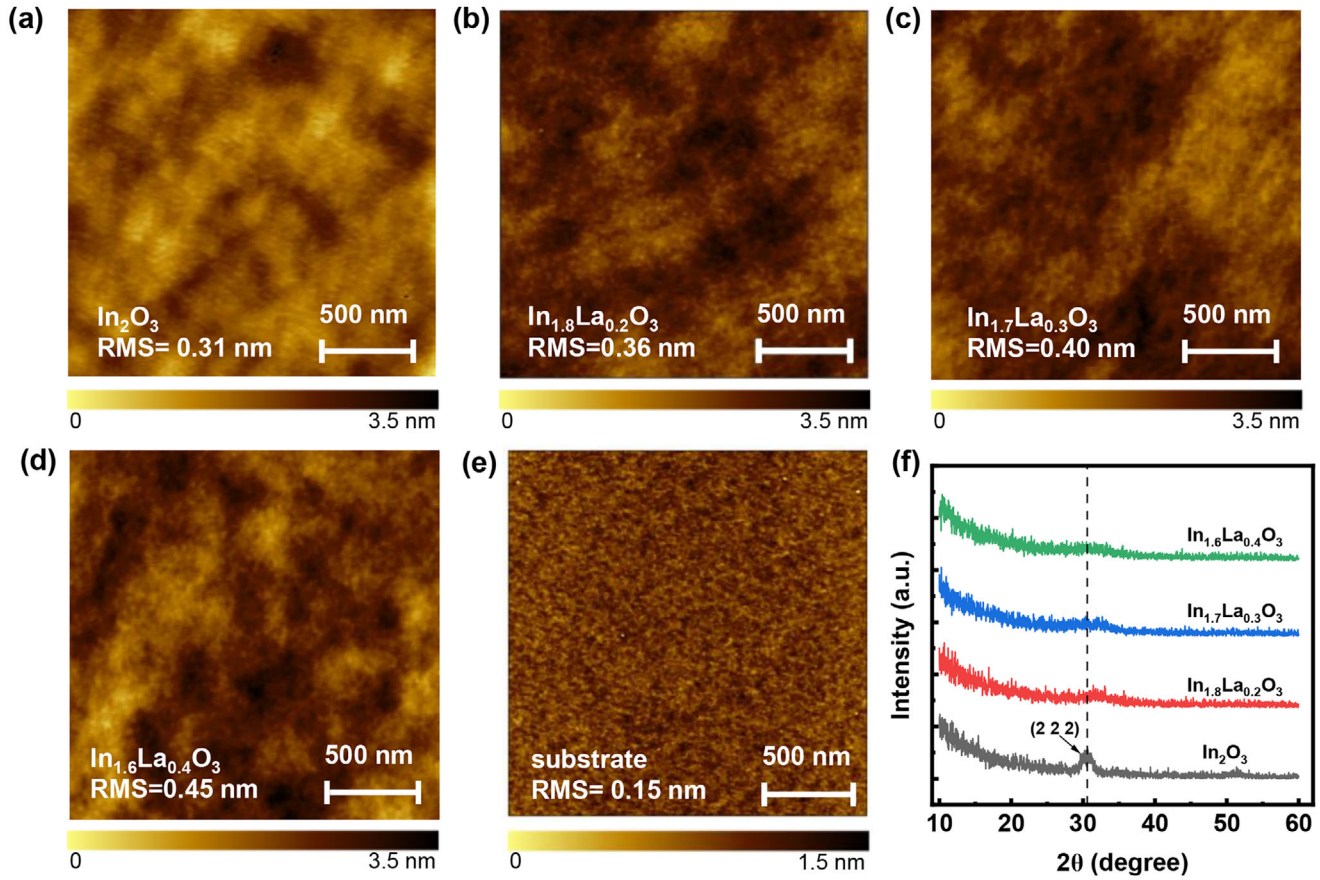

FIGURE 1 | AFM surface morphology images of (a–d) as-deposited InLaO films with different La concentrations and (e) Si substrate. (f) XRD patterns of the InLaO films with different La concentration 400°C annealing in O_2 for 10 min.

In order to further explore the components and chemical states of InLaO films, XPS was carried out, as shown in Figure 2. No distinct binding energy shift is observed in the In 3d and La 3d of different InLaO samples (Figure 2a–d), indicating the formation of In—O and La—O bonding in the InLaO films. Furthermore, to analyze oxygen-metal bonding, the O 1s peak is deconvoluted into three subpeaks. The subpeaks centered at 529.56–529.59, 530.28–530.34, and 531.5–531.65 eV, which are related to oxygen in metal oxides (M-O), V_O, and metal hydroxide species (M—OH), respectively, are shown in Figure 2e–h. As seen in Figure 2d, the area radio of $V_O/(V_O$+M-O+M—OH) after the introduction of La decreases from 24.0% to 15.94%. This result indicates the excellent ability of La^{3+} in suppressing the formation of V_O, which is directly attributed to the stronger La—O bonding strength compared to In—O bonding.

2.2 | Electrical Performance of InLaO TFTs

To investigate the effect of La concentration on electrical performance, devices with different La concentrations were fabricated, the schematic of the TFT is shown in Figure 3a. Figure 3b presents the transfer curves at V_{DS} = 0.1 V with a channel length (L) of 10 μm. The excellent subthreshold swing (SS) values (72–77 mV dec^{-1}) benefit from the high-quality interface between the ALD-grown HfO_2 GI and the InLaO channel, which is further confirmed by the double-sweep transfer curves measured at V_{DS} = 0.1 and 1.2 V (Figure 4e–h) showing negligible hysteresis. The corresponding field-effect mobility (μ_{FE}) and threshold voltage (V_{TH}), extracted from the transfer curves at V_{DS} = 0.1 V, are shown in Figure 3c. The In_2O_3 TFT shows high μ_{FE} (106.3 $cm^2(V{\cdot}s)^{-1}$) and highly negative V_{TH} (−1.35 V), which suggesting a very conductive channel. As the La concentration increases from 10.8 to 20.2 at. %, the μ_{FE} decreases from 41.2 to 2.3 $cm^2(V{\cdot}s)^{-1}$, and V_{TH} shifts positively from −0.83 to 1.16 V. This trend is corroborated with the output curves in Figure 4e–h, which show a reduction in drain current (I_{DS}) at the same gate voltage, indicating lower channel conductivity. Based on the XPS and XRD results, it can be inferred that the less conductive channel can be attributed to the La-induced amorphization and the suppression of V_O (which acts as a shallow donor), due to stronger La—O bonding. Besides, TFTs with different L are shown in Figure 5, In_2O_3 TFTs suffer from significant short-channel effects (negative V_{TH} roll-off and SS degradation), InLaO TFTs maintain stable V_{TH}, μ_{FE}, and SS with L down to 5 μm, demonstrating that La incorporation enhances the scalability.

2.3 | Bias Stability of InLaO TFTs

The modulation of channel properties by La doping has been established through basic electrical characterization. To further evaluate the impact of reliability, the bias stability is systematically investigated, as shown in Figure 6. The positive-bias-stress (PBS) and negative-bias-stress (NBS) conditions were $V_{stress} = \pm 1$, 2, and 3 V in vacuum at room temperature for 1000 s, respectively.

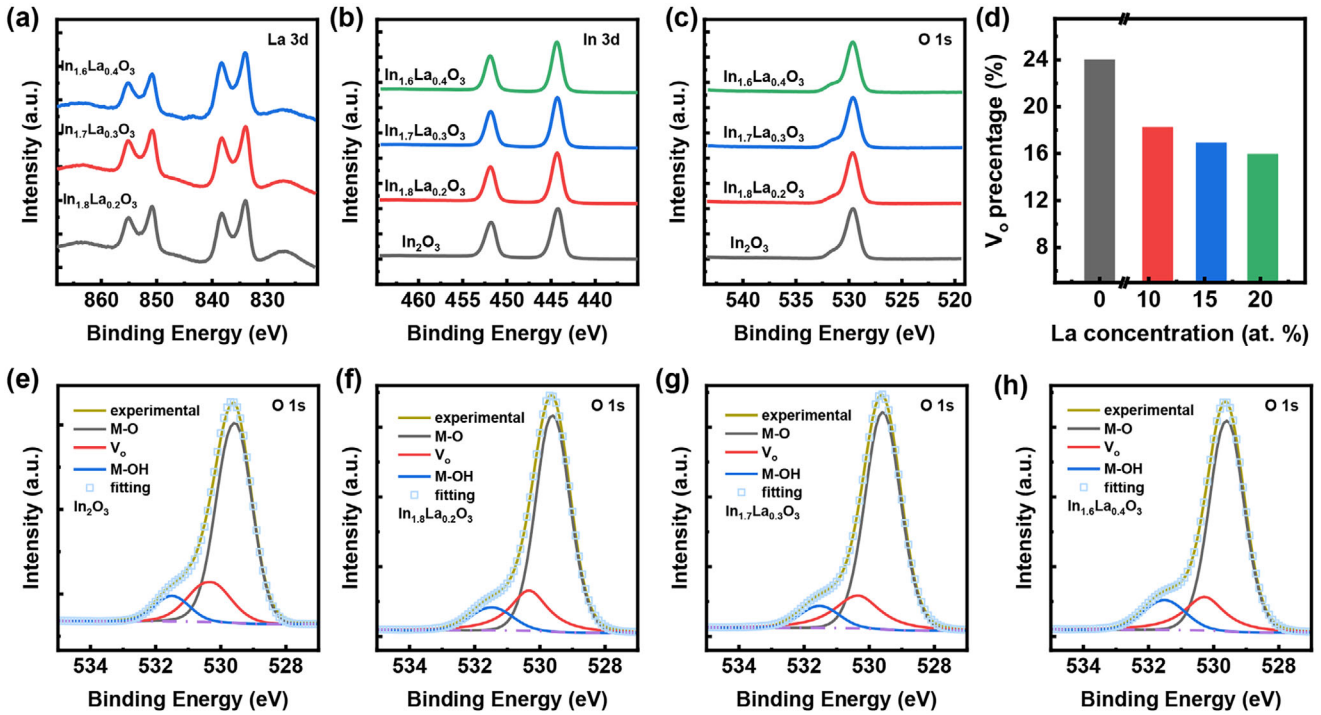

FIGURE 2 | (a–c) In 3d, La 3d and O 1s XPS spectra of InLaO thin films with different La concentration, (d) V_O ratio in InLaO thin films with different La concentration extracted from (e–h) deconvoluted O 1s XPS spectra.

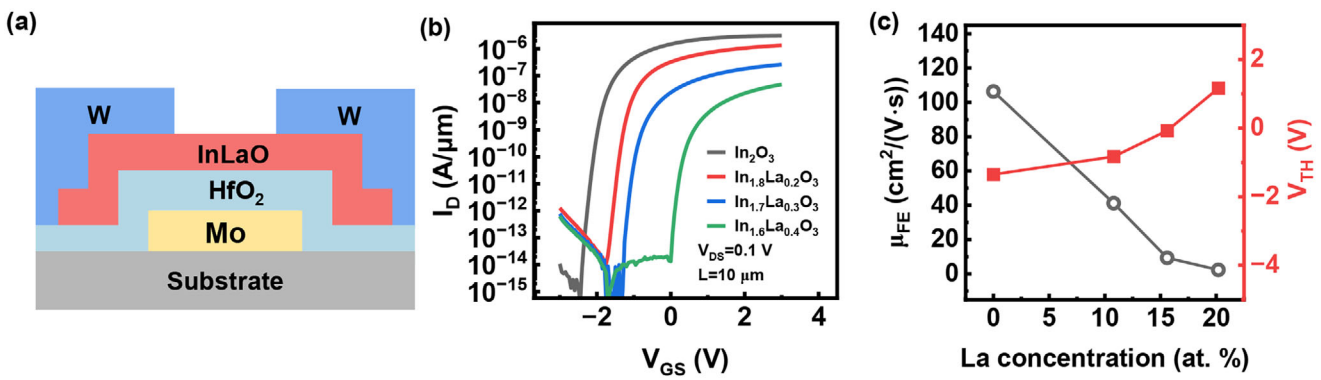

FIGURE 3 | (a) The schematic cross-section of a bottom-gate and top-contact InLaO transistor. (b) Transfer curves of the InLaO transistors with different La concentrations. (c) μ_{FE} and V_{TH} extracted from (b).

As shown in Figure 6a–c, the undoped In_2O_3 TFTs exhibit a negative ΔV_{TH} under PBS from 1 to 3 V. However, with light La doping, the ΔV_{TH} shifts to positive at the higher V_{stress} of 3 V. This result implicates that the negative ΔV_{TH} in In_2O_3 is directly attributed to the donor defects in the channel, especially $V_O \rightarrow V_O^{2+} + 2e^-$. La incorporation effectively suppresses this mechanism. This conclusion corresponds with the XPS results, which show a decreasing V_O concentration with increasing La content. The suppression mechanism originates from the stronger La—O bonding, which stabilizes the oxide lattice against the field-assisted breaking of the weaker In—O bonds and the subsequent formation of V_O under PBS. Besides, with further increase in La concentration, the positive ΔV_{TH} under 3 V, PBS becomes larger, as shown in Figure 6d. This indicates that while moderate La doping suppresses bulk V_O-related instability, a new degradation pathway becomes dominant at high La content. This positive shift is attributed to enhanced charge trapping at the GI or the channel/GI interface. While La doping suppresses oxygen vacancy-related defects in the channel bulk, the stability under PBS at high La concentrations can be limited by the degradation of the channel/GI interface. This interface degradation may generate traps, which capture electrons under PBS and lead to a positive ΔV_{TH}. Excessive La doping, despite its efficiency in passivating V_O, can degrade high-field stability, highlighting the need for optimal doping concentration. Meanwhile, the same negative ΔV_{TH} observed under low-field PBS (V_{stress} = 1 and 2 V) for both undoped and lightly La-doped samples suggests a common defect. In addition to V_O, hydrogen, commonly incorporated during ALD growth, could contribute to negative ΔV_{TH}. Hydrogen may exist as interstitial hydrogen

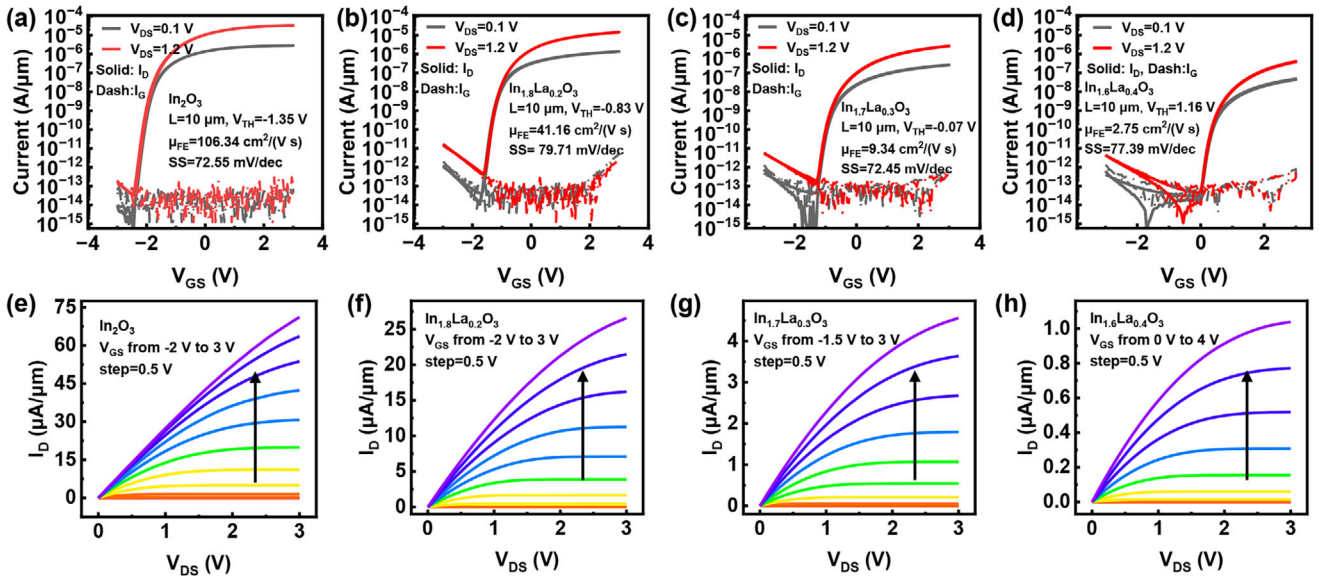

FIGURE 4 | (a–d) The double-sweep I_D-V_{GS} and I_G-V_{GS} curves measured at V_{DS} = 0.1 and 1.2 V, and (e–h) corresponding output curves of the InLaO transistors with different La concentration.

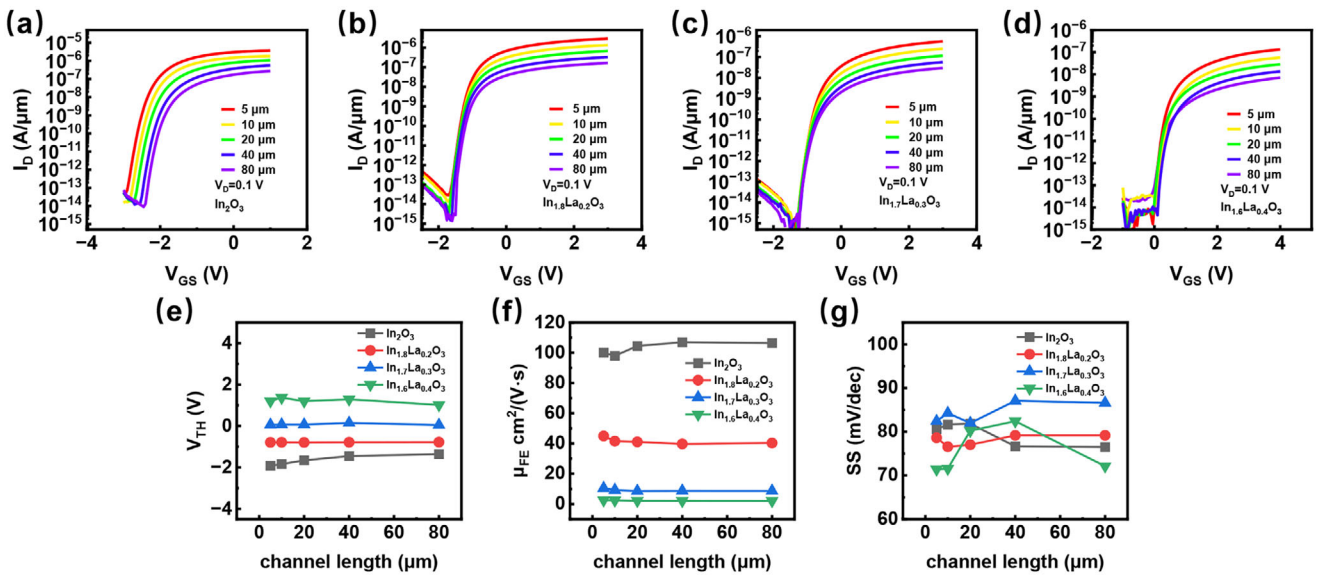

FIGURE 5 | Transfer characteristics of the (a–d) In_2O_3 and InLaO TFTs with different L. (e–f) V_{TH}, $μ_{FE}$, and SS extracted from the corresponding TFTs.

or substitutional hydrogen in V_O, under positive bias, hydrogen can act as an electron donor, and leading to negative ΔV_{TH}. La-doping effectively suppresses oxygen vacancy formation and consequently reduces the concentration of both V_O-related and hydrogen-related donors.

The NBS stability of InLaO TFTs was shown in Figure 6e–h, and the NBS of the devices was significantly improved with La doping. Under NBS of V_{stress} = −3 V, the ΔV_{TH} systematically decreases from −0.58 to −0.36, −0.16, and finally to −0.01 V with increasing La concentration, as shown in Figure 6e–h. The improvement in NBS stability directly results from the suppression of V_O by the stronger La—O bonds, as shown in Figure 7. Besides, the $In_{1.6}La_{0.4}O_3$ TFTs show an initial positive shift followed by a gradual reversal to a negative shift, suggesting the existence of more than once mechanisms with different time constants. The positive shift is much smaller than the stability gains from La doping. Consequently, this phenomenon does not influence the conclusion of the effective enhancement of bias stability via La-induced defect passivation.

Table 2 benchmarks the performance of InLaO TFTs in this study with other reported InLaO TFTs [23–27]. A wider range of La doping concentrations was achieved by ALD, and the SS values as low as ~70 mV dec^{-1} are significantly lower than those reported in other works, benefiting from the high-quality

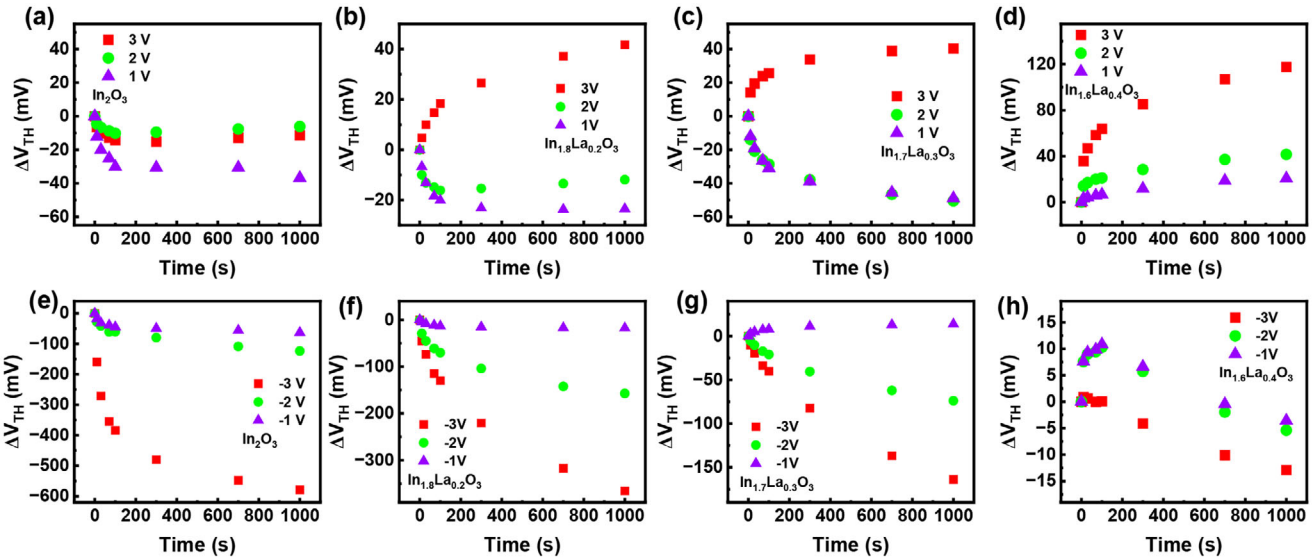

FIGURE 6 | Bias stress instabilities of the InLaO transistors with (a–d) PBS and (e–h) NBS. The PBS and NBS stress conditions are $V_{GS} = \pm 1$, 2, and 3 V at room temperature for 1 ks.

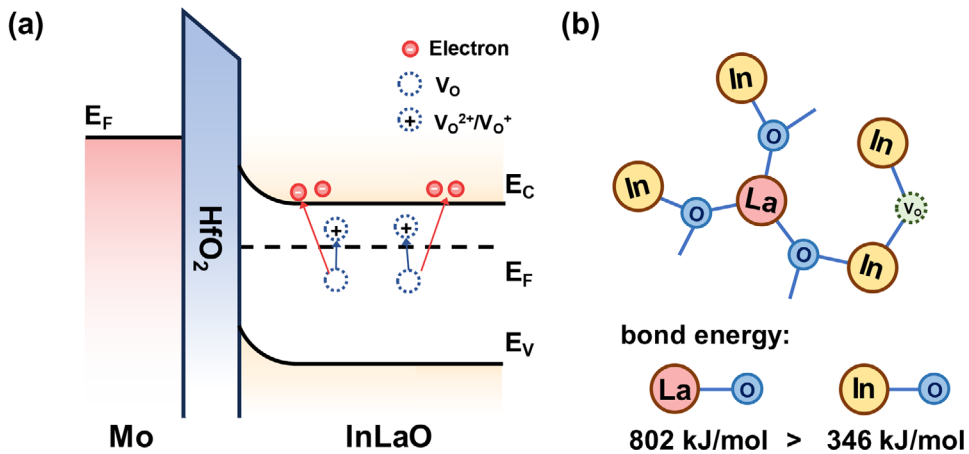

FIGURE 7 | (a) Mechanisms of the negative bias instability. Donor-like traps and oxygen vacancies ($V_O \rightarrow V_O^{2+} + 2e^-$, $V_O \rightarrow V_O^+ + e^-$) under NBS release electrons, resulting in a negative shift of V_{TH}. (b) Schematic diagram of InLaO structure, illustrating the suppression of V_O due to strong La—O bonding after doping.

interface between the ALD-grown gate dielectric and channel. Under a high V_{stress}/EOT (equivalent oxide thickness) value of 5.6 MV/cm, the ΔV_{TH} is remarkably small ($\Delta V_{TH} < 0.1$ V). Meanwhile, NBS stability is enhanced with increasing La content, ultimately reaching a negligible shift of −0.005 V. These results demonstrate the superior interfacial quality and exceptional bias-stress stability achieved through ALD-engineered La doping in In_2O_3 TFTs.

3 | Conclusions

This study systematically investigates the impact of La doping in ALD-grown In_2O_3 for the first time. InLaO thin films were characterized by comprehensive characterization, and these results are in accordance with the electrical performances of corresponding TFTs. The strong La—O bonding leads to the suppression of V_O, resulting in a decrease in μ_{FE} from 106.3 to 2.3 $cm^2(V{\cdot}s)^{-1}$ coupled with a positive V_{TH} shift from −1.35 to 1.16 V. Benefiting from ALD, the devices exhibit excellent SS values as low as ~70 mV dec^{-1}. Meanwhile, the PBS and NBS of the InLaO TFTs were also evaluated, $In_{1.6}La_{0.4}O_3$ TFT represents excellent bias stability, such as ΔV_{TH} of −0.042 and −0.005 V under ±2 V for 1ks. These results establish ALD-grown La doping as an effective V_O suppression and pave the way for the exploitation of La-doped In_2O_3 devices.

4 | Experimental Section

4.1 | InLaO Film and TFT Fabrication Methods

The InLaO thin films were deposited by ALD with (3-(dimethylamino)propyl)-dimethyl indium (DADI) and

TABLE 2 | Benchmarking of the relevant InLaO TFT devices, including mobility, V_{TH}, SS, EOT, and bias stress stabilities [23–27].

Film Technique	La [at.%]	μ [$cm^2(V{\cdot}s)^{-1}$]	V_{TH} [V]	SS [V/dec]	Measurement condition [a]	PBS ΔV_{TH} (V)	NBS ΔV_{TH} (V)	EOT (nm)	Refs.
Sputter	5	34.7	−3.4	0.19	PBS: 10 V, 1 h NBS: −10 V, 1 h V_{stress}/EOT = 1.2 MV/cm	0.20	−0.6	83.9	[23]
Solution	0	48.8	1.12	0.33	PBS: 2.5 V, 1 h	0.21	0.21	9.7	[24]
	1	42.3	1.26	0.22	NBS: −3 V, 1 h	0.50	0.14		
	4.8	36.5	1.41	0.15	V_{PBS}/EOT = 2.6 MV/cm	0.36	0.10		
	9.1	32.7	1.76	0.12	V_{NBS}/EOT = 3.1 MV/cm	0.19	0.08		
nanofiber	0	7.5	−4.1	1.09	PBS: V_{GS}-V_{TH} = 2 V, 1 h	13.52	—	100	[25]
	2	5.3	−0.6	0.98	V_{stress}/EOT = 0.2 MV/cm	6.10	—		
	5	5.0	4.5	0.51		2.90	—		
	8	1.2	6.66	0.5		0.38	—		
solution	5	3.5	−4.1	—	PBS: 20 V, 1 h NBS: −20 V, 1 h 60°C V_{stress}/EOT = 2.2 MV/cm E = 2.2 MV/cm	2.90	0.5	90.5	[26]
solution	0	22.5	0.8	0.13	PBS: 2 V, 1 h	0.17	−0.08	11.3	[27]
	0.5	21	1.2	0.75	NBS: −2 V, 1 h	0.13	−0.03		
	1	5	1.5	0.09	V_{stress}/EOT = 1.8 MV/cm	—	—		
	3	2.5	1.7	0.09		—	—		
ALD	0	106.3	−1.35	0.073	PBS: 2 V, 1 ks	−0.006	−0.120	3.6	[this work]
	10.8	41.2	−0.83	0.079	NBS: −2 V, 1 ks	−0.074	−0.157		
	15.6	9.3	−0.07	0.072	V_{stress}/EOT = 5.6 MV/cm	0.050	−0.074		
	20.2	2.3	1.16	0.077		0.042	−0.005		

[a]Measurement condition includes stress voltage, time, and V_{stress}/EOT.

tris(N,N′-diisopropylformamidinato) lanthanum ($La(^iPrfAMD)_3$) with ozone (O_3) as the oxidant at 225°C. And the metal precursors were held at 60 and 150°C, respectively. The metal precursor pulse times were 0.3 s for DADI and 0.5 s for $La(^iPrfAMD)_3$, followed by corresponding O_3 pulse times of 0.1 and 0.5 s. For the deposition using each precursor, N_2 gas was used as purge gas with a purge time of 20 s. The ALD super-cycle consisted of n values of 0, 5, 10, and 15, corresponding to the samples denoted as In_2O_3, $In_{1.8}La_{0.2}O_3$, $In_{1.7}La_{0.3}O_3$, and $In_{1.6}La_{0.4}O_3$, respectively. The InLaO TFTs with a bottom-gate and top-contact structure were fabricated on a Si wafer with 90 nm thermally grown SiO_2. A 50 nm Mo was used as the gate electrode by magnetron sputtering, after which an 8-nm HfO_2 gate dielectric was grown by ALD. The channels (InLaO and In_2O_3) were deposited by ALD using the above-mentioned films, and patterned with dilute hydrochloric acid at a ratio of 1:10. The post-deposition annealing process for the TFT was conducted for 10 min at 400°C in O_2. Finally, magnetron sputtering was used to deposit 50 nm tungsten (W) as the source and drain (S/D) electrodes, which were patterned using UV lithography and lift-off processes. The channel width and length were 40 and 10 μm, respectively.

4.2 | Analysis Methods

The electrical properties were evaluated using a Keysight 1500 semiconductor parameter analyzer in vacuum conditions (~1 mPa) and at room temperature to avoid any influence from the ambient environment. The bias stability was measured in a dark and vacuum environment, and a constant stress voltage (±1, 2, and 3 V) was applied to the TFTs. The degradation was monitored by intermittently interrupting the stress at 10, 30, 70, 100, 300, 500, and 1000 s to perform a fast transfer characteristic measurement at V_D = 0.1 V. The V_{TH} was extracted from each of the transfer curves using the constant-current method shown in Figure S1. Capacitance-voltage (C–V) measurements were performed on metal-insulator-metal (MIM) capacitors using a Keysight 4980 LCR meter at the frequency from 1 kHz to 1 MHz with a small AC signal amplitude of 30 mV. The C–V characteristics measured are presented in Figure S2, with the corresponding capacitor structure illustrated in the inset. The extracted unit-area capacitance (C_{ox}) at the minimum of the C–V curve is 9.7×10^{-3} F/m^2, and the extracted EOT is 3.6 nm. The thickness of as-deposited oxide films was measured by spectroscopic ellipsometry. The roughness

of the as-deposited thin films was characterized by AFM (Cypher S, Asylum Research). In addition, the crystallinity of the films annealing in 400°C O_2 was analyzed by GIXRD (Smartlab, Rigaku). Chemical bond states were analyzed by XPS (AXIS Ultra DLD, Kratos), which was carried out using a monochromatic Al Kα (1486.6 eV) source.

Acknowledgements

This work was supported by the National Natural Science Foundation of China under Grants 62274107, 92264204, and Shanghai Pilot Program for Basic Research-Shanghai Jiao Tong University under Grant 21TQ1400212.

Conflicts of Interest

The authors declare no conflicts of interest.

Data Availability Statement

The data that support the findings of this study are available from the corresponding author upon reasonable request.

References

1. K. Nomura, H. Ohta, A. Takagi, T. Kamiya, M. Hirano, and H. Hosono, "Room-temperature Fabrication of Transparent Flexible Thin-film Transistors Using Amorphous Oxide Semiconductors," *Nature* 432 (2004): 488–492, https://10.1126/science.1083212.

2. M. Kim, J. H. Jeong, H. J. Lee, et al., "High Mobility Bottom Gate InGaZnO Thin Film Transistors with SiO_x Etch Stopper," *Applied Physics Letters* 90 (2007): 21, https://doi.org/10.1063/1.2742790.

3. H. H. Hsieh, H. H. Lu, H. C. Ting, C. S. Chuang, C. Y. Chen, and Y. Lin, "Development of IGZO TFTs and Their Applications to Next-Generation Flat-Panel Displays," *Journal of Information Display* 11 (2010): 160–164, https://doi.org/10.1080/15980316.2010.9665845.

4. G. J. Lee, J. Kim, J.-H. Kim, S. M. Jeong, J. E. Jang, and J. Jeong, "High Performance, Transparent a-IGZO TFTs on a Flexible Thin Glass Substrate," *Semiconductor Science and Technology* 29 (2014): 035003, https://doi.org/10.1088/0268-1242/29/3/035003.

5. H.-J. Shin, S. Takasugi, K.-M. Park, et al., "7.1: Invited Paper: Novel OLED Display Technologies for Large-Size UHD OLED TVs," *SID Symposium Digest of Technical Papers* 46 (2015): 53–56, https://doi.org/10.1002/sdtp.10225.

6. Y. Zhu, Y. He, S. Jiang, L. Zhu, C. Chen, and Q. Wan, "Indium–Gallium–Zinc–Oxide Thin-Film Transistors: Materials, Devices, and Applications," *Journal of Semiconductors* 42 (2021): 031101, https://doi.org/10.1088/1674-4926/42/3/031101.

7. M. Si, Z. Lin, Z. Chen, X. Sun, H. Wang, and P. D. Ye, "Scaled Indium Oxide Transistors Fabricated Using Atomic Layer Deposition," *Nature Electronics* 5 (2022): 164–170, https://doi.org/10.1038/s41928-022-00718-w.

8. Z. Wang, J. Zhao, K. Jiang, et al., "O_3-ZnO Superlattice Transistors by Atomic Layer Deposition with High Field-Effect Mobility," *IEEE Electron Device Letters* 46 (2025): 412–415, https://doi.org/10.1109/LED.2025.3532673.

9. J. Troughton and D. Atkinson, "Amorphous InGaZnO and Metal Oxide Semiconductor Devices: An Overview and Current Status," *Journal of Materials Chemistry C* 7 (2019): 12388–12414, https://doi.org/10.1039/C9TC03933C.

10. J. Song, X. Huang, C. Han, Y. Yu, Y. Su, and P. Lai, "Recent Developments of Flexible InGaZnO Thin-Film Transistors," *Physica Status Solidi (A)* 218 (2021): 2000527, https://doi.org/10.1002/pssa.202000527.

11. M. Kimura and S. Imai, "Degradation Evaluation of α-IGZO TFTs for Application to AM-OLEDs," *IEEE Electron Device Letters* 31 (2010): 963–965, https://doi.org/10.1109/LED.2010.2052235.

12. Y. G. Mo, M. Kim, C. K. Kang, et al., "Amorphous-Oxide TFT Backplane for Large-Sized AMOLED TVs," *Journal of the Society for Information Display* 19 (2011): 16–20, https://doi.org/10.1889/JSID19.1.16.

13. K. Ide, K. Nomura, H. Hosono, and T. Kamiya, "Electronic Defects in Amorphous Oxide Semiconductors: A Review," *Physica Status Solidi (A)* 216 (2019): 1800372, https://doi.org/10.1002/pssa.201800372.

14. D. Geng, K. Wang, L. Li, et al., "Thin-film Transistors for Large-area Electronics," *Nature Electronics* 6 (2023): 963–972, https://doi.org/10.1038/s41928-023-01095-8.

15. H. Bae, S. Jun, C. H. Jo, et al., "Modified Conductance Method for Extraction of Subgap Density of States in a-IGZO Thin-film Transistors," *IEEE Electron Device Letters* 33 (2012): 1138–1140, https://doi.org/10.1109/LED.2012.2198870.

16. M. Si, A. Charnas, Z. Lin, and P. D. Ye, "Enhancement-mode Atomic-layer-deposited in_2O_3 Transistors with Maximum Drain Current of 2.2 A/Mm at Drain Voltage of 0.7 V by Low-temperature Annealing and Stability in Hydrogen Environment," *IEEE Transactions on Electron Devices* 68 (2021): 1075–1080, https://doi.org/10.1109/TED.2021.3053229.

17. O. Bierwagen, "Indium Oxide—A Transparent, Wide-Band Gap Semiconductor For (Opto)Electronic Applications," *Semiconductor Science and Technology* 30 (2015): 024001, https://doi.org/10.1088/0268-1242/30/2/024001.

18. M. Si, Y. Hu, Z. Lin, et al., "Why In_2O_3 Can Make 0.7 nm Atomic Layer Thin Transistors," *Nano Letters* 21 (2020): 500–506, https://doi.org/10.1021/acs.nanolett.0c03967.

19. S. Parthiban and J.-Y. Kwon, "Role Of Dopants As A Carrier Suppressor And Strong Oxygen Binder In Amorphous Indium-Oxide-Based Field Effect Transistor," *Journal of Materials Research* 29 (2014): 1585–1596, https://doi.org/10.1557/jmr.2014.187.

20. Y. G. Kim, T. Kim, C. Avis, S.-H. Lee, and J. Jang, "Stable and High-performance Indium Oxide Thin-film Transistor by Ga Doping," *IEEE Transactions on Electron Devices* 63 (2016): 1078–1084, https://doi.org/10.1109/TED.2016.2518703.

21. A. Abliz, L. Xu, D. Wan, et al., "Effects Of Yttrium Doping On The Electrical Performances And Stability Of Zno Thin-Film Transistors," *Applied Surface Science* 475 (2019): 565–570, https://doi.org/10.1016/j.apsusc.2018.12.236.

22. Y. Zhang, H. Zhang, J. Yang, X. Ding, and J. Zhang, "Solution-Processed Yttrium-Doped IZTO Semiconductors For High-Stability Thin Film Transistor Applications," *IEEE Transactions on Electron Devices* 66 (2019): 5170–5176, https://doi.org/10.1109/TED.2019.2949702.

23. P. He, H. Xu, L. Lan, et al., "The Effect of Charge Transfer Transition on the Photostability of Lanthanide-doped Indium Oxide Thin-film Transistors," *Communications Materials* 2 (2021): 86, https://doi.org/10.1038/s43246-021-00193-4.

24. Z. Lin, L. Lan, P. Xiao, et al., "Effects of Rare-Earth Element Dopants in High-mobility InO_x-based Thin-film Transistors," *IEEE Electron Device Letters* 37 (2016): 1139–1142, https://doi.org/10.1109/LED.2016.2593485.

25. C.-Y. Zhao, J. Li, D.-Y. Zhong, et al., "Effect of La Addition on the Electrical Characteristics and Stability of Solution-Processed LaInO Thin-Film Transistors With High-k ZrO_2 Gate Insulator," *IEEE Transactions on Electron Devices* 65 (2017): 526–532, https://doi.org/10.1109/TED.2017.2781725.

26. Q. Chen, J. Li, Y. Yang, W. Zhu, and J. Zhang, "Combustion Synthesis of Electrospun LaInO Nanofiber for High-performance Field-effect Transistors," *Nanotechnology* 30 (2019): 425205, https://doi.org/10.1088/1361-6528/ab306d.

27. W. Wang, G. He, H. Yu, et al., "Enhanced Electrical Performance and Stability of La-Doped Indium Oxide-Based Thin-Film Transistors and Application Explorations," *Physica Status Solidi (A)* 219 (2022): 2100590, https://doi.org/10.1002/pssa.202100590.

28. W. Wang, G. He, Y. Li, et al., "All-solution-driven Thin-film Transistor with Low Power Dissipation for Logic Electronics and Neuronal Synapse," *IEEE Transactions on Electron Devices* 70 (2023): 3590–3597, https://doi.org/10.1109/TED.2023.3276728.

29. H. Du, K. Tuokedaerhan, and R. Zhang, "Electrical Performance of La-doped In_2O_3 Thin-film Transistors Prepared Using a Solution Method for Low-voltage Driving," *RSC Advances* 14 (2024): 15483–15490, https://doi.org/10.1039/D4RA01409J.

30. M. Zeng, S. Yan, S. Liu, T. Fu, Q. Hu, and Y. Wu, "First Demonstration of High-Temperature Reliability on La: HZO-La: In_2O_3 FeFET with High Endurance of 10^{10} at 125°C," *IEEE Electron Device Letters* 46 (2025): 1632–1635, https://doi.org/10.1109/LED.2025.3587573.

31. Q. Gao, G. He, B. He, et al., "High-Performance Neuromorphic Phototransistors Based on Electrospinning-Driven La-Doped Indium Oxide Nanofibers," *IEEE Transactions on Electron Devices* 72 (2025): 4969–4975, https://doi.org/10.1109/TED.2025.3589341.

32. B. Lee, T. Park, A. Hande, et al., "Electrical Properties of Atomic-layer-deposited La_2O_3 Films Using a Novel La Formamidinate Precursor and Ozone," *Microelectronic Engineering* 86 (2009): 1658, https://doi.org/10.1016/j.mee.2009.03.05.

33. W. Maeng, D.-W. Choi, J. Park, and J.-S. Park, "Indium Oxide Thin Film Prepared by Low Temperature Atomic Layer Deposition Using Liquid Precursors and Ozone Oxidant," *Journal of Alloys and Compounds* 649 (2015): 216–221, https://doi.org/10.1016/j.jallcom.2015.07.150.

34. Y. Li, D. Zhu, W. Xu, et al., "High-Mobility Nanometer-Thick Crystalline In–Sm–O Thin-Film Transistors Via Aqueous Solution Processing," *Journal of Materials Chemistry C* 8 (2020): 310–318, https://doi.org/10.1039/C9TC05162G.

35. W. Hume-Rothery, "Researches on the nature, properties, andconditions of formation of intermetallic compounds, with special reference tocertain compounds of tin," Doctoral dissertation (University of London, 1926).

Supporting Information

Additional supporting information can be found online in the Supporting Information section.

Supporting File: adma72778-sup-0001-SuppMat.docx.